Journal of Applied Physics ARTICLE pubs.aip.org/aip/jap

Domain switching and shear-mode piezoelectric response induced by cross-poling in polycrystalline ferroelectrics

Cite as: J. Appl. Phys. **136**, 194101 (2024); doi: 10.1063/5.0238994
Submitted: 16 September 2024 · Accepted: 31 October 2024 ·
Published Online: 15 November 2024

View Online Export Citation CrossMark

D. A. Hall,[1,a)] L. Daniel,[2,3] M. Watson,[4] A. Condie,[4] T. P. Comyn,[5] A. K. Kleppe,[6] and P. J. Withers[1,7]

AFFILIATIONS

[1]Department of Materials, University of Manchester, Oxford Rd., Manchester M13 9PL, United Kingdom
[2]Université Paris-Saclay, CentraleSupélec, CNRS, Laboratoire de Génie Électrique et Électronique de Paris, Gif-sur-Yvette 91192, France
[3]Sorbonne Université, CNRS, Laboratoire de Génie Électrique et Électronique de Paris, Paris 75252, France
[4]Xaar plc, 316 Cambridge Science Park, Cambridge CB4 0XR, United Kingdom
[5]Ionix Advanced Technologies Ltd., Lynthorne House, Intercity Way, Leeds, West Yorkshire LS13 4LX, United Kingdom
[6]Diamond Light Source Ltd, Harwell Science and Innovation Campus, Didcot, Oxfordshire OX11 0DE, United Kingdom
[7]Henry Royce Institute, University of Manchester, Oxford Rd., Manchester M13 9PL, United Kingdom

[a)]**Author to whom correspondence should be addressed:** david.a.hall@manchester.ac.uk

ABSTRACT

The mechanisms contributing to the electromechanical response of piezoelectric ceramics in the shear mode have been investigated using high-energy synchrotron x-ray diffraction. Soft lead zirconate titanate ceramic specimens were subjected to an electric field in the range 0.2–3.0 MV m^{-1}, perpendicular to that of the initial poling direction, while XRD patterns were recorded in transmission. At low electric field levels, the axial strains remained close to zero, but a significant shear strain occurred due to the reversible shear-mode piezoelectric coefficient. Both the axial and shear strains increased substantially at higher field levels due to irreversible ferroelectric domain switching. Eventually, the shear strain decreased again as the average remanent polarization became oriented toward the electric field direction. The lattice strain and domain orientation distributions follow the form of the total strain tensor, enabling the domain switching processes to be monitored by the rotation of the principal strain axis. Reorientation of this axis toward the electric field direction occurred progressively above 0.6 MV m^{-1}, while the angle of rotation increased from 0° to approximately 80° at the maximum field of 3.0 MV m^{-1}. A strong correlation was established between the effective strains associated with different crystallographic directions, which was attributed to the effects of elastic coupling between grains in the polycrystal.

I. INTRODUCTION

Lead zirconate titanate (PZT) ceramics find widespread applications in electromechanical sensors, actuators, and transducers.[1–5] In the majority of cases, these devices are designed to utilize the axial piezoelectric charge/strain coefficients, d_{33} and d_{31}, with the electric field applied along the poling axis X_3, to create the required form of electromechanical response. Typical examples include multilayer piezoelectric stack actuators, in which a longitudinal strain is induced by an applied electric field via d_{33}, and patch actuators, in which a transverse strain is induced via d_{31}, or equivalently d_{32}.[1,6,7] In contrast, the utilization of the shear mode, via d_{15} or d_{24}, is less common, although the piezoelectric activities of many commercial piezoceramics in shear can be substantially higher in magnitude than those of the axial cases.[8,9]

Applications of shear-mode piezoelectric devices include accelerometers, which take advantage of the de-coupling of piezoelectric and pyroelectric responses, non-destructive testing, energy

harvesting, and industrial inkjet printheads.[10–12] Shear-mode devices can benefit from the higher dielectric and piezoelectric coefficients, in comparison with axial modes, although the lower coercive field can lead to re-poling or *cross-poling*, along the direction perpendicular to that of the initial remanent polarization vector and consequent degradation of the device performance.[13–15]

The nonlinear piezoelectric properties of a commercial PZT shear-mode actuator were reported by Malakooti and Sodano,[16] who utilized a novel digital image correlation (DIC) technique to determine the piezoelectric shear strain in response to an applied electric field in the range from 0 to 0.6 MV m^{-1}. Under a bipolar AC electric field waveform, the d_{15} coefficient increased from approximately 1300 to 2700 pm V^{-1}, suggesting an increasing extrinsic ferroelectric domain switching contribution to the field-induced strain. Furthermore, the relationship between d_{15} and electric field amplitude was approximately linear over this range of field strength, in accordance with the empirical Rayleigh law, as reported previously for the direct and converse piezoelectric effects in the axial modes.[17–19]

The underlying mechanisms that contribute to the piezoelectric behavior of poled ferroelectric ceramics in shear mode have received relatively little attention[13,20] in contrast to the case for the axial modes where many studies have been conducted to establish how the nonlinear dielectric and piezoelectric responses are affected by factors such as the crystal structure, microstructure, chemical composition, and environment.[18,21–23] Further studies of material behavior and device design for shear-mode sensors and actuators are now required to explore the potential for enhanced electromechanical responses. From the perspective of lead-free piezoceramics development, the utilization of the shear mode provides an additional opportunity to compensate for the generally weaker piezoelectric activity of such materials[8,24,25] and to explore novel types of thick film technologies.[26,27]

The development of diffraction methods for the study of ferroelectric domain switching and related phenomena, utilizing state of the art synchrotron x-ray and neutron sources to sample bulk properties, has provided new insights into the actuation mechanisms in ferroelectric ceramics.[28–31,32] *In situ* synchrotron XRD measurements have revealed the importance of elastic constraint in coupling together the nominally *intrinsic* lattice strain and *extrinsic* domain switching mechanisms in polycrystalline ferroelectrics,[33–35] while significant deviations from the average strain were identified at the local grain scale by 3D-XRD.[36] Similar methods have also been employed to investigate the novel strain-generating mechanisms in lead-free relaxor ferroelectrics, including those based on sodium bismuth titanate solid solutions, which involve nanopolar to long-range ordered ferroelectric transitions and changes in crystal symmetry under the influence of an applied electric field.[37–39,40] However, to date there have been no such investigations of domain switching or local lattice strain in the shear mode, although an *ex situ* study of cross-poling textures in a tetragonal PZT was reported by Wan and Bowman.[41]

The aim of the present study was to determine the orientation-dependent changes in lattice strain and ferroelectric domain orientation for a commercial soft PZT ceramic in response to an electric field applied in a direction perpendicular to the poling axis. It is shown that the initially dominant shear strain is transformed into a combination of axial and shear strains as the magnitude of the electric field increases toward and beyond the coercive field. The methods described in the present work allow the orientation of the remanent polarization in ferroelectric ceramics to be monitored and controlled; this approach facilitates the investigations of the orientation-dependent piezoelectric coefficients and could lead to the development of novel piezoelectric devices with optimized piezoelectric responses.

II. EXPERIMENTAL METHODS

Commercial soft PZT ceramics were provided by Xaar in the form of non-electroded wafers, with a thickness of 0.9 mm. These had previously been poled perpendicular to the major surfaces, along the X_3 direction. Square-ended beam-shaped specimens with dimensions of 3×1 mm^2 were cut from these wafers by diamond machining. Electrodes were then applied to the end faces of the specimens, normal to the X_1 direction, using air-drying silver paint (Electrolube SCP03B). Using this procedure, an electric field applied lengthways, along X_1, is perpendicular to the through-thickness poling direction, X_3, as illustrated in Fig. 1(a).

XRD measurements were performed in transmission at beamline I15 of Diamond Light Source using high-energy, monochromatic x rays with a photon energy of 67 keV corresponding to a wavelength of 0.1839 Å. A schematic diagram of the beam–sample–detector geometry is illustrated in Fig. 1(a), where it is evident that the beam direction is perpendicular to both the electric field and the initial remanent polarization vectors. In the conventional arrangement for a piezoelectric ceramic actuator, in which the electric field is usually applied in a direction parallel to the poling axis, transverse isotropy can be assumed and it is then relatively straightforward to obtain the full strain tensor by the analysis of the 2D diffraction patterns, corresponding to a range of different azimuthal angles, ψ, relative to the electric field axis. This approach is no longer valid in the present case due to the application of the electric field along direction X_1 and the consequent loss of the fiber-like symmetry due to the progressive and irreversible cross-poling process.

Two-dimensional images of the diffraction pattern were recorded using a Perkin-Elmer XRD 1621 flat-panel detector positioned approximately 1 m from the sample, as shown in Fig. 1(b). These images were reduced ("caked") into conventional one-dimensional XRD patterns corresponding to a range of grain orientations, ψ, relative to the poling direction, using Fit2D.[42] Calibration was performed with a LaB_6 powder standard. The peak profiles for selected diffraction peaks were fitted to one or more pseudo-Voigt functions, using a least-square errors procedure in MATLAB, in order to quantify the lattice spacings and integrated peak intensities.

XRD patterns were recorded *in situ*, during the application of an electric potential in the range from 0 to ±9 kV along direction X_1, using a Trek 610E HV amplifier, the specimen being immersed in silicone oil within a polyimide oil bath during the experiments to prevent arcing between the electrodes. The amplifier was controlled remotely from the beamline computer system by means of a low-level analog voltage so that the XRD data and applied electric field could be correlated. The measurement procedure consisted of

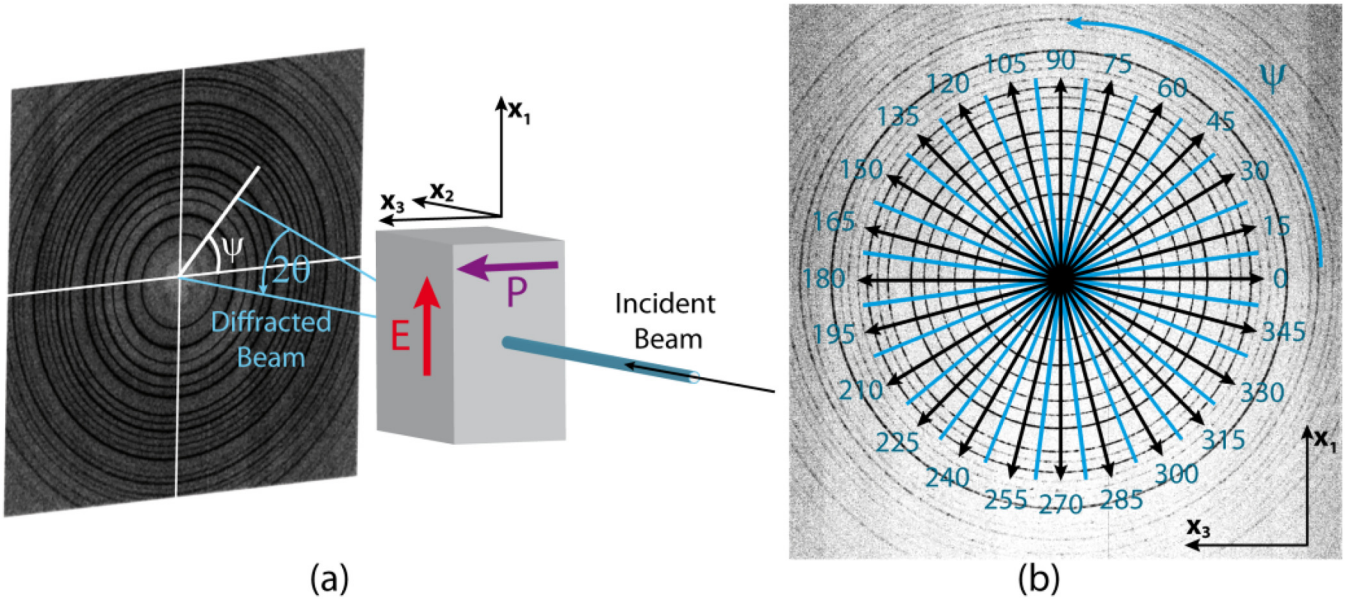

FIG. 1. (a) Schematic diagram of the beam–sample–detector geometry for high-energy XRD measurements in transmission, showing directions of initial remanent polarization and applied electric field vectors. (b) Illustration of the 2D diffraction pattern showing how the arcs are "caked" into 24 azimuthal bins.

applying a sequence of gradually increasing quasi-static bipolar electric field levels in a stepwise manner, including measurements in the remanent state at zero electric field between the positive and negative levels, as illustrated in Fig. 2. It was anticipated that the maximum field level of $\pm 3\,\mathrm{kV\,mm^{-1}}$ would be sufficient to completely re-polarize the specimen along the electric field direction, since its magnitude was more than twice the coercive field of this type of soft PZT ceramic.

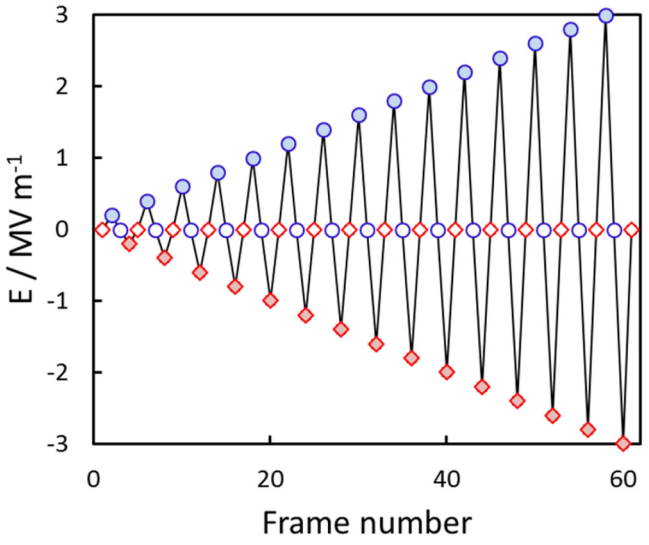

FIG. 2. Illustration of measurement procedure involving step-wise application of a quasi-static bipolar electric field. Four different datasets were obtained, corresponding to the specimen under an increasing positive or negative electric field (filled symbols) and including their respective remanent states (open symbols).

III. RESULTS

A. Characterization of the initial poled state

A typical XRD pattern obtained for $\psi = 0°$, with the scattering vector along the initial poling direction (X_3), is presented in Fig. 3. Splitting of the {h00} diffraction peaks is clearly evident, indicating a predominantly tetragonal crystal structure. A 2-peak fitting procedure yielded consistent results for the {200} and {220} reflections while a single peak profile provided a good fit to {111}.

Peak profiles for the {111}, {200}, and {220} reflections in the initial poled state are illustrated in Fig. 4. Systematic variations in the peak positions and intensities as a function of azimuthal angle, ψ, are clearly evident in these plots. The results indicate a preference for c-axis oriented domains, represented by the (002) peak, along X_3 at $\psi = 0°$, with a reversal in the relative intensities of the (002) and (200) peaks occurring for $\psi = 90°$. Similar systematic variations in peak intensities can be observed for the {220} reflections. The corresponding shifts in the position of the {111} peak with variations in ψ indicate the development of tensile lattice strain along X_3 and compressive strain along X_1 during poling. These poling strains along ⟨111⟩ in the remanent state are caused by elastic constraint and intergranular residual stresses within the polycrystal, which couples together the extrinsic (domain switching) and intrinsic (lattice strain) mechanisms, as discussed previously.[33,35]

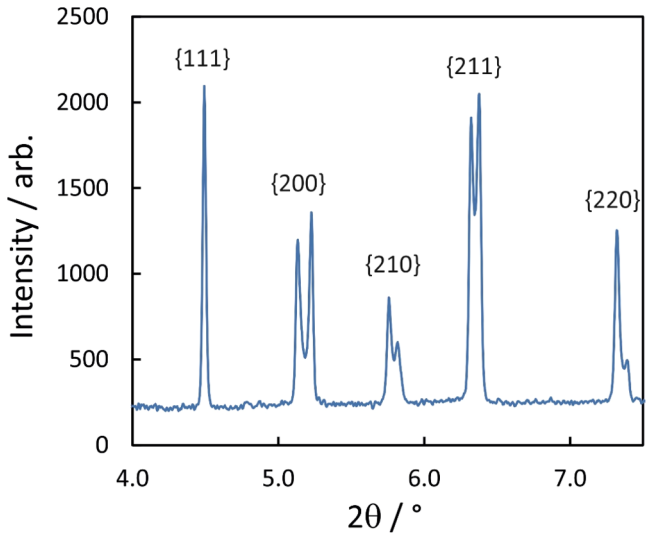

FIG. 3. 1D diffraction pattern of poled commercial PZT ceramic for the scattering vector along the initial poling direction, with $\psi = 0°$, corresponding to a typical tetragonal perovskite structure.

One of the aims of our analysis is to determine the lattice strain orientation distribution and domain orientation distribution (SOD and DOD, respectively) under the influence of a cross-poling field along X_1. For this purpose, it is necessary to provide values for the lattice spacing, d_{111}, and the diffraction peak intensity ratios, R_{002} and R_{202}, in the unpoled, randomly textured state. The fractional peak intensity ratios are defined as follows:

$$R_{002} = \frac{I_{002}}{I_{002} + I_{200}}, \tag{1}$$

$$R_{202} = \frac{I_{202}}{I_{202} + I_{220}}, \tag{2}$$

where I_{hkl} denotes the intensity of the corresponding diffraction peak. However, these values were not readily available since the specimens were provided in a pre-poled condition. Therefore, they were determined instead by making use of the near-linear relationships between these parameters and $\cos^2\psi$, illustrated in Fig. 5, which result from the form of the strain tensor associated with domain reorientation.[33] The reference parameters d^0_{111}, R^0_{002}, and R^0_{202} were identified as their respective values at the point where $\cos^2\psi = 1/3$, determined as 0.234 334 nm, 0.305, and 0.653,

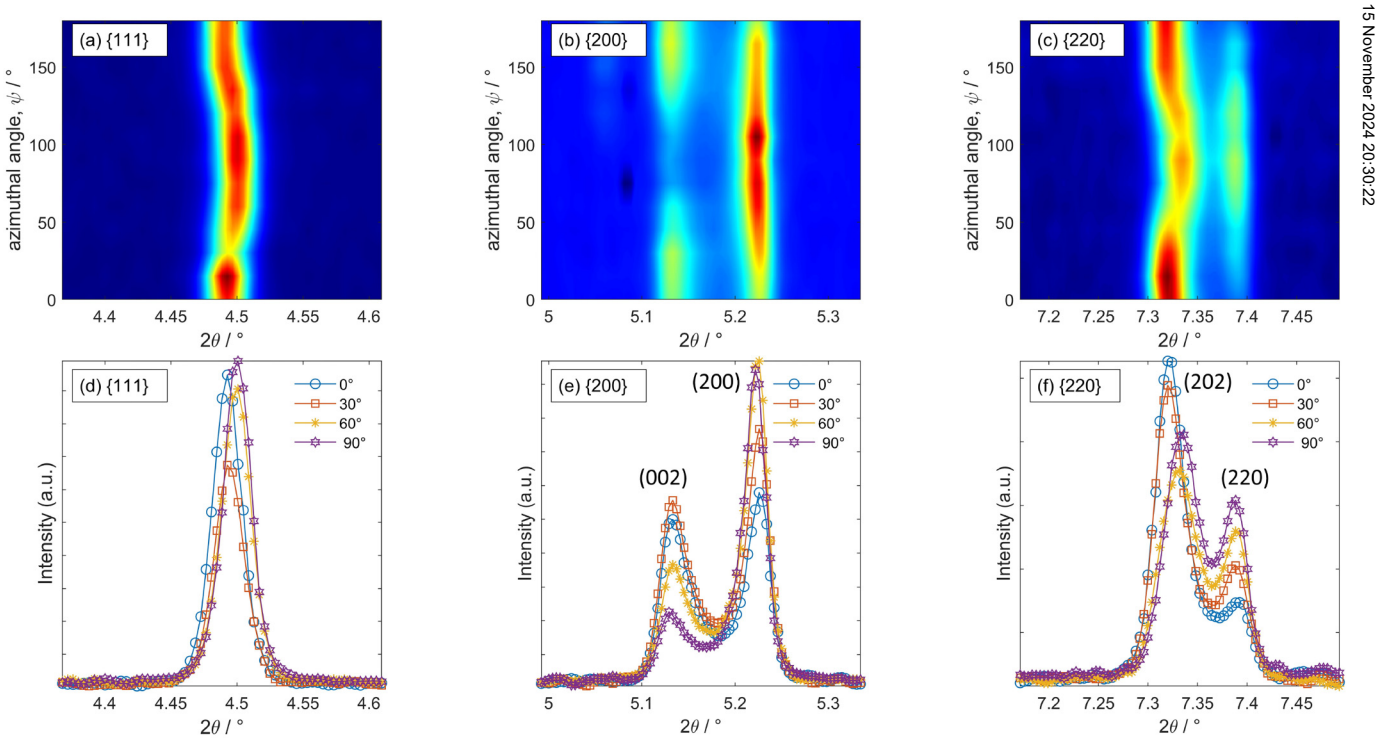

FIG. 4. Variations in diffraction peak profiles for (a) {111}, (b) {200}, and (c) {220} reflections of pre-poled tetragonal PZT ceramic as a function of azimuthal angle, ψ. Line profiles for selected orientations are shown in (d)–(e).

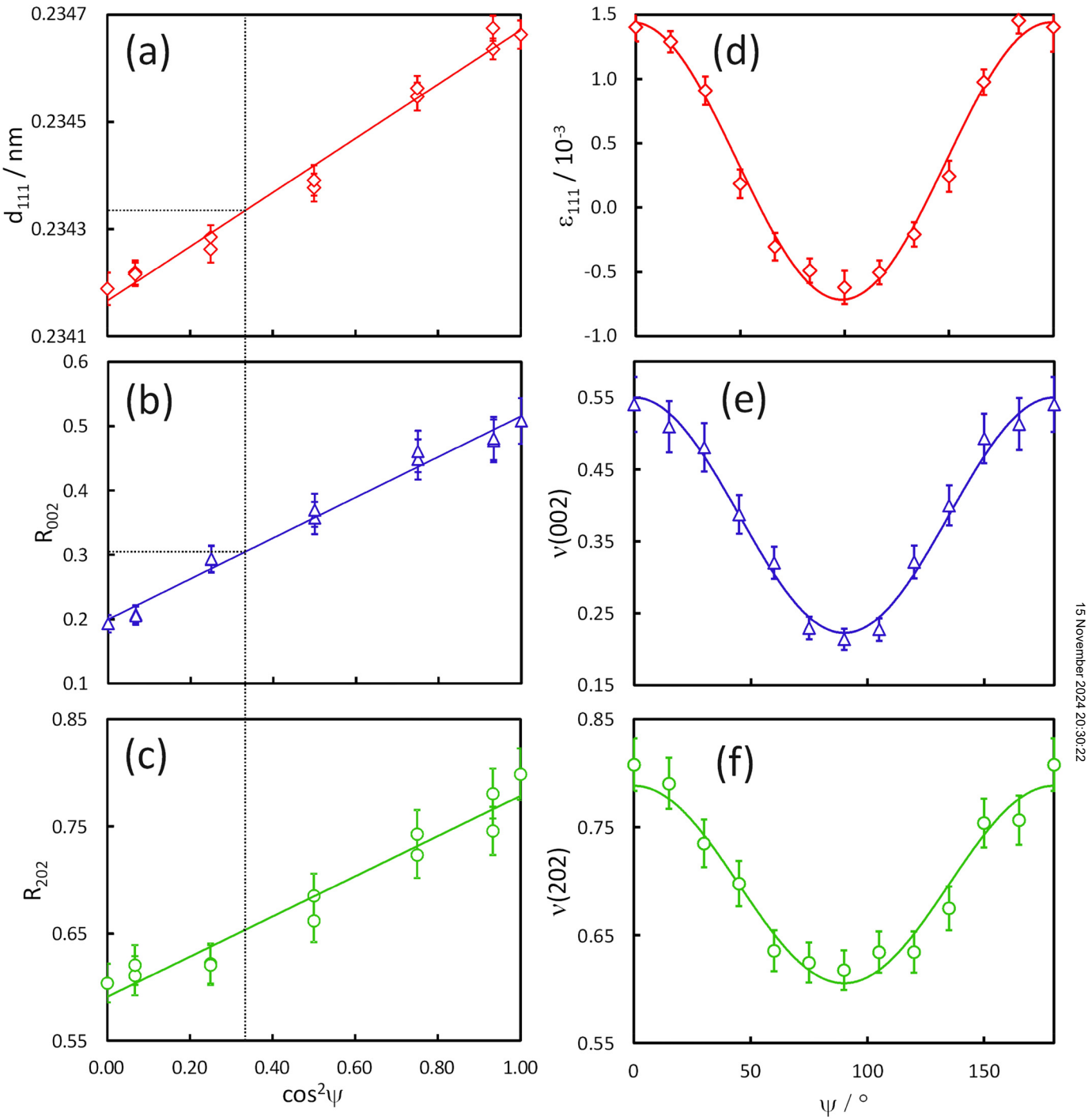

FIG. 5. Characterization of the initial poled state. Variations in (a) the lattice parameter, d_{111}, and peak intensity ratios, (b) R_{002} and (c) R_{202}, with azimuthal angle, ψ. The values of the respective parameters at the orientation for which $\cos^2\psi = 1/3$ were used to represent the stress- and texture-free state. The corresponding strain and domain orientation distributions (SOD and DOD, respectively) are shown in (d) to (f).

respectively (see Fig. 5). Note that this point represents the orientation at which the total axial strain component, $\varepsilon(\psi)$, is equal to zero, which is assumed to represent the strain- and texture-free state with random domain orientation.[29]

The relative intensity ratios for the 002/200 and 202/022 doublets are defined as

$$W_{002} = \frac{I_{002}}{I_{200}}, \tag{3}$$

$$W_{202} = \frac{I_{202}}{I_{022}}. \tag{4}$$

The reference values of W^0_{002} and W^0_{202} in the unpoled randomly oriented state were obtained from the previously determined R^0_{002} and R^0_{202} values using the following relationships:

$$W^0_{002} = \frac{R^0_{002}}{(1 - R^0_{002})}, \tag{5}$$

$$W^0_{202} = \frac{R^0_{202}}{(1 - R^0_{202})}. \tag{6}$$

The SOD and DOD functions for each family of lattice planes are calculated using the method described by Jones *et al.*,[43]

$$\varepsilon_{\{111\}}(\psi) = \frac{d_{111} - d^0_{111}}{d^0_{111}}, \tag{7}$$

$$\nu_{002}(\psi) = \frac{I_{002}/I^0_{002}}{I_{002}/I^0_{002} + 2\ I_{200}/I^0_{200}}, \tag{8}$$

$$\nu_{202}(\psi) = \frac{2\ I_{202}/I^0_{202}}{2\ I_{202}/I^0_{202} + \ I_{220}/I^0_{220}}. \tag{9}$$

Here, parameters ν_{002} and ν_{202} represent the relative fractions of domains oriented along [002] and [202], respectively. The expressions given in (8) and (9) were simplified and expressed in terms of the relative intensity ratios, W_{002} and W_{202},

$$\nu_{002}(\psi) = \frac{1}{1 + 2\ W^0_{002}/W_{002}}, \tag{10}$$

$$\nu_{202}(\psi) = \frac{2}{2 + \ W^0_{202}/W_{202}}. \tag{11}$$

The resulting SOD and DOD functions, illustrating the development of tensile lattice strain and preferred domain orientation along the initial poling direction ($\psi = 0$), are presented in Figs. 5(d)–5(f).

B. Effects of the cross-poling electric field

The effects of an applied bipolar electric field with progressively increasing amplitude from 0.2 to 3.0 MV m^{-1} are illustrated by the diffraction peak profiles shown in Fig. 6, which are derived from diffraction patterns having the scattering vector parallel to the cross-poling electric field, i.e., $\psi = 90°$. The gradual shift of the {111} peak to lower 2θ values indicates the development of tensile lattice strain along the electric field axis, while the reversal of relative intensities in the {200} and {220} doublets demonstrates the reorientation of ferroelectric domains toward the electric field direction. There is also clear evidence of partial "back-switching" of domains, accompanied by relaxation of the lattice strain, between the "field-on" and "field-off" states. Complementary data for $\psi = 0$, 45, and 135° are presented in Figs. S1–S3 in the supplementary material, while the variations in the peak profiles as a function of ψ in the final remanent state are illustrated in Fig. S4 in the supplementary material.

To quantify the effects of the applied electric field, the weighted average effective lattice strains for {200} and {220}, $\varepsilon_{\{hkl\}}$, were calculated using the respective lattice parameters and DOD functions, as follows:[44]

$$d_{\{200\}}(\psi) = \ \nu_{002} d_{002} + (1 - \nu_{002}) d_{200}, \tag{12}$$

$$d_{\{220\}}(\psi) = \ \nu_{202} d_{202} + (1 - \nu_{202}) d_{220}, \tag{13}$$

$$\varepsilon_{\{hkl\}}(\psi) = \frac{d_{hkl} - d^0_{hkl}}{d^0_{hkl}}. \tag{14}$$

Note that this approach does not attempt to distinguish between the intrinsic and extrinsic contributions, arising from the lattice strain and ferroelectric domain switching respectively, unlike that used in certain other publications.[35,44,45] Instead, the $\varepsilon_{\{200\}}$ and $\varepsilon_{\{220\}}$ values combine the lattice strains with the transformation strain from domain switching into an effective total lattice strain associated with a given plane family. The resulting SOD functions in the remanent state, after the application of various cross-poling electric fields, are presented in Fig. 7. For the initial state, it is evident that all grain orientations exhibit the maximum (positive) strain along X_3 ($\psi = 0°$) and the minimum (negative) strain along X_1 ($\psi = 90°$). These results are a consequence of the macroscopic changes in strain during poling, which give rise to tensile and compressive strains along X_3 and X_1, respectively.

Furthermore, the lattice strains are anisotropic, with $\varepsilon_{\{200\}}$ having the highest magnitude, $\varepsilon_{\{111\}}$ having the lowest, and $\varepsilon_{\{220\}}$ being intermediate. This trend is similar to that described previously for tetragonal PZT ceramics;[44] it can be explained in terms of the transformation strains associated with domain switching during poling and their dependence on crystallographic orientation.[33] The {100} and {111} grain families represent the two extreme cases for a tetragonal perovskite crystal since the spontaneous polarization lies along ⟨100⟩, yielding the largest transformation strain from domain switching, while ⟨111⟩ is insensitive to domain switching and therefore has zero transformation strain. For a polycrystalline tetragonal perovskite ferroelectric in the remanent poled state, the {111} lattice strain can be attributed solely to the effects of residual stress caused by elastic constraint, i.e., it is a response to the macroscopic poling strain.[33]

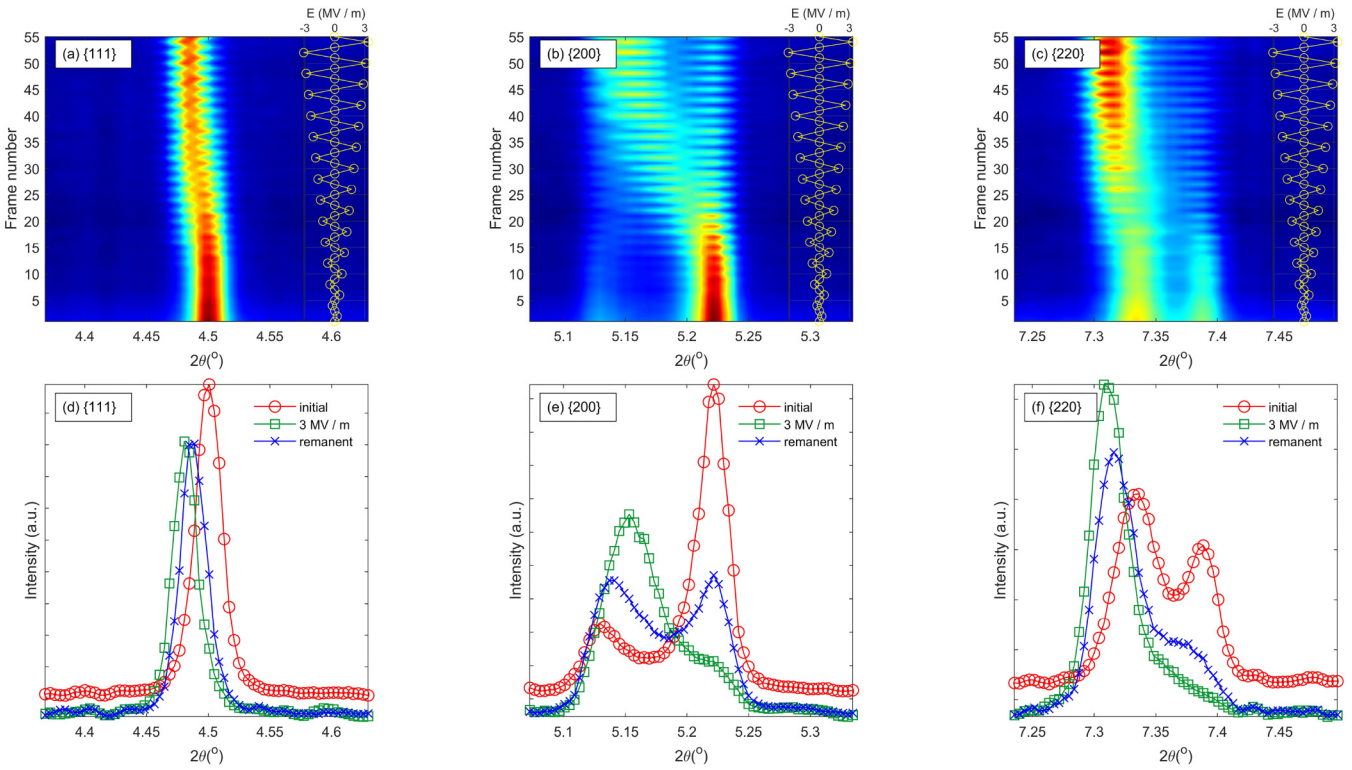

FIG. 6. Influence of the bipolar electric field on the (a) {111}, (b) {200}, and (c) {220} diffraction peak profiles, represented as contour plots, for the azimuthal angle $\psi = 90°$ (scattering vector parallel to E). Peak profiles corresponding to the initial state, under the highest electric field level and in the remanent state are compared in (d)–(f).

The application of an electric field along X_1, perpendicular to the initial poling direction, led to progressive shifts in the directions associated with the maximum and minimum strains, as illustrated in Figs. 7(b) and 7(c). These effects are attributed to domain switching along X_1, which gives rise to an effective rotation of the average remanent polarization direction. It is evident that the maximum positive strains were obtained at ψ values of approximately 0°, 45°, and 80° for electric field levels of 0, 1.4, and 3.0 MV m^{-1}, respectively. Additionally, it was found that the magnitudes of the maximum and minimum peak strain values, which represent the principal strains, increase slightly during the course of the experiment; this indicates that the degree of domain alignment at the conclusion of the experiment was greater than that at the start. It was observed that the maximum values of ν_{002} increased from 0.55 to 0.60, while those of ν_{202} increased from 0.79 to 0.89 after the application of 3 MV m^{-1} along X_1. This point is discussed further in Sec. III D.

Although the lattice strains for each family of reflections retain their heterogeneous nature during and after cross-poling, the azimuthal orientations, ψ, associated with the maximum and minimum strains shift in a consistent manner with the increasing electric field strength. The latter observation indicates a correlation between the SODs associated with different crystallographic orientations, which is a further indication of the strong elastic coupling between grains in polycrystalline ferroelectrics. Otherwise, it might be anticipated that the {002}-oriented grains would exhibit domain switching at a lower electric field level than that of the {220}-oriented grains, for example. Elastic coupling between domain switching and lattice strain in the sub-coercive field range was also emphasized by Pramanick *et al.*[35] In contrast, it has been found in certain metallic alloys that differently oriented grain families can exhibit plastic strain at different loading levels, referred to as *plastic anisotropy*.[46]

C. Total strain: Deformation and piezoelectric response

The evolution of the total strain during the course of the experiment was evaluated by combining the results for the effective lattice strains, following the approach described by Daymond.[47,48] This yields an estimate for the total strain, $\varepsilon^*(\psi)$, in terms of a weighted average incorporating the multiplicities of the different lattice planes, m_{hkl}, as

$$\varepsilon^*(\psi) = \frac{\sum_{hkl} T_{hkl} m_{hkl} \varepsilon_{hkl}(\psi)}{\sum_{hkl} T_{hkl} m_{hkl}}. \quad (15)$$

The m_{hkl} values for the representative {111}, {200}, and {220} grain families are 8, 6, and 12, respectively, and it is assumed that the texture index, T_{hkl}, is equal to 1 in each case. This latter assumption supposes that the crystal (grain) orientations in the

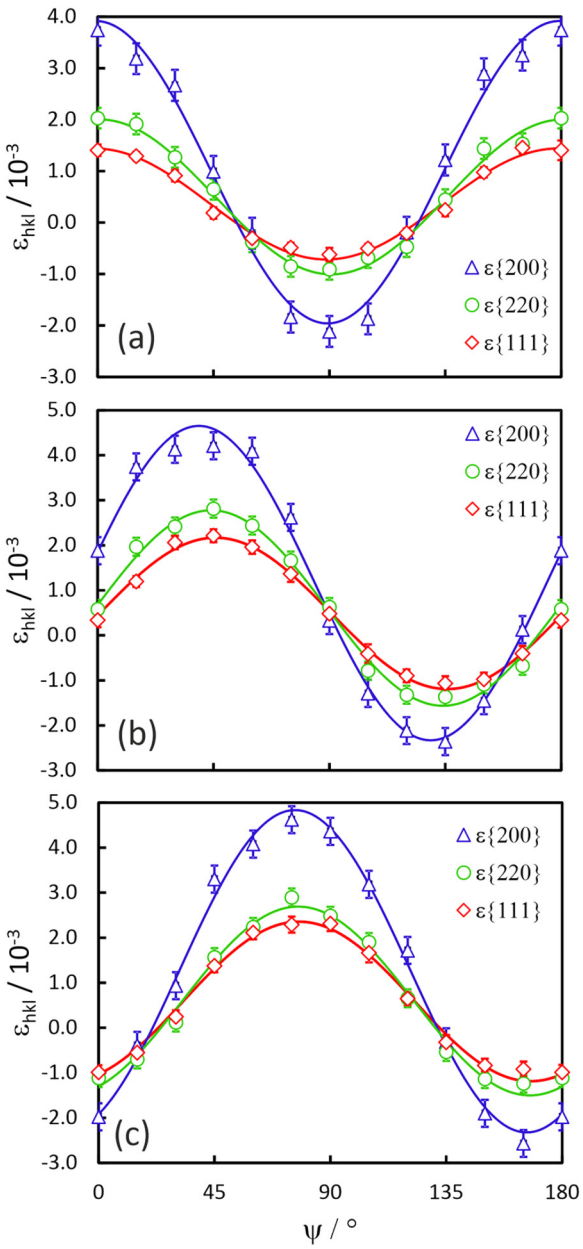

FIG. 7. Changes in effective strain orientation distribution (SOD) for different crystallographic directions in the remanent state after application of a cross-poling field with magnitude (a) 0, (b) 1.4, and (c) 3 MV m^{-1}. Solid lines represent the best fit according to Eq. (16).

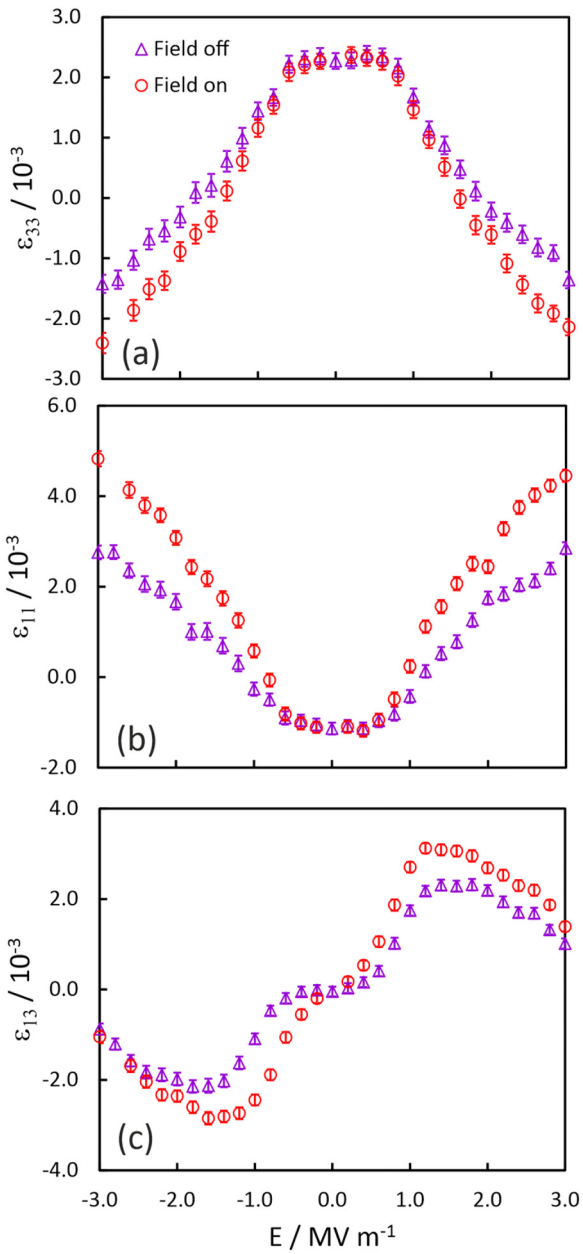

FIG. 8. Field-dependence of (a) ε_{33}, (b) ε_{11}, and (c) ε_{13} total strain tensor components under an increasing bipolar electric field, illustrating results obtained under field, denoted as "field-on," and in the remanent state, "field-off."

material are perfectly random. Equation (15) relies on the assumption of locally isotropic elastic properties for the single crystal. It was shown by Daniel *et al.*[49] that elastic anisotropy can be a significant factor in PZT ceramics, but it is believed that the intrinsic and extrinsic piezoelectric effects remain as the dominant features in the observed behavior. A more refined definition of the total strain would require knowledge of the elastic properties of the material and the use of more elaborate micro-mechanical modeling tools. It should also be noted that the definition of $\varepsilon^*(\psi)$ corresponds solely to the strain components associated with the 1–3 plane, which is

the only one accessible according to the experimental configuration illustrated in Fig. 1(a). Consequently, the full strain tensor cannot be obtained using this beam–sample–detector geometry, which limits our analysis to the axial, ε_{11} and ε_{33}, and shear, ε_{13}, strain components.

The total SOD given by Eq. (15) was subsequently fitted to the standard strain tensor transformation (16) in order to provide the strain corresponding to each electric field level,

$$\varepsilon^{*}(\psi) = \varepsilon_{33} + (\varepsilon_{11} - \varepsilon_{33})sin^{2}\psi + 2\varepsilon_{13}\, sin\psi\, cos\psi. \quad (16)$$

The evolution of these parameters during the cross-poling experiment is illustrated by the results presented in Fig. 8. At low electric field levels, for $E < 0.8\ MV\ m^{-1}$, the axial components, ε_{11} and ε_{33}, remained close to zero, as is expected for a piezoelectric specimen in the shear mode. A relatively small and reversible change occurred in the shear component, ε_{13}, which is attributed to the shear piezoelectric response. At higher electric field levels, for $E > 0.8\ MV\ m^{-1}$, large and irreversible changes in both axial and shear strains are evident due to ferroelectric domain switching, resulting in progressive cross-poling along the electric field direction. The axial strain components, ε_{11} and ε_{33}, together with the differences between the "field-on" and "field-off" states, $\Delta\varepsilon_{11}$ and $\Delta\varepsilon_{33}$, continued to increase in magnitude up to the maximum applied field of $3\ MV\ m^{-1}$, while the shear component, ε_{13}, first increased but then subsequently saturated and reduced. The comparison of the results obtained for different crystallographic orientations, presented in Fig. S5 in the supplementary material, shows that the largest strains are obtained consistently for {200}, followed by {220} and finally {111}, over the full range of applied electric field levels.

Although these results provide an indication of the changes in piezoelectric activity induced by the cross-poling procedures, detailed interpretation is hindered by the strongly nonlinear nature of the piezoelectric response. For example, the observed changes in the $\Delta\varepsilon_{ij}$ values with increasing electric field are caused by both the reorientation of the remanent polarization and the field-dependence of the effective piezoelectric coefficients. Nevertheless, the progressive increase in the axial piezoelectric coefficients due to cross-poling along X_1 is clearly evident in Fig. 8.

The $\Delta\varepsilon_{ij}$ values were subsequently employed to estimate the effective piezoelectric coefficients, d_{ij}^{*}, over a range of different field levels. The ultimate d_{33}^{*} and d_{31}^{*} values were approximately +800 and $-350\ pm\ V^{-1}$, which are in general agreement with the macroscopic piezoelectric coefficients of soft PZT ceramics, indicating that the specimen was poled predominantly along X_1 at the conclusion of the experiment. Note that the standard notation is used here to represent the indices for d_{33}^{*} and d_{31}^{*}, which differs from that employed in the discussion above in that the directions of X_1 and X_3 are interchanged.

The results obtained for ε_{13} appear to indicate significant increases in the shear strain for electric field levels up to $1.2\ MV\ m^{-1}$, declining thereafter. This observation suggests that a certain degree of cross-poling could potentially enhance the shear-mode piezoelectric activity. However, it should be noted that these changes are substantially irreversible and are a consequence of the rotation of the average polarization vector toward the electric field direction. This point can be clarified by examining the variations in the difference strain, $\Delta\varepsilon_{13}$, as a function of the electric field, as shown in Fig. 9. The $\Delta\varepsilon_{13}$–E relationship appears to be approximately linear up to $0.8\ MV\ m^{-1}$, after which it decays. The linear part of the curve exhibited a gradient of approximately $1.00 \times 10^{-9}\ m\ V^{-1}$, which yields an effective piezoelectric shear strain coefficient, d_{15}^{*}, of $2.00 \times 10^{-9}\ m\ V^{-1}$ after taking into consideration the factor of 2 required for conversion into the conventional Voigt notation.[50] The apparently linear nature of the shear strain–electric field relationship in this region is in conflict with previous observations of nonlinearity.[13,16] However, the uncertainty in the data obtained at low fields is relatively high and, therefore, further *in situ* diffraction studies of the sub-coercive field region, similar to those conducted previously in the axial mode,[35,45] could help to clarify this point.

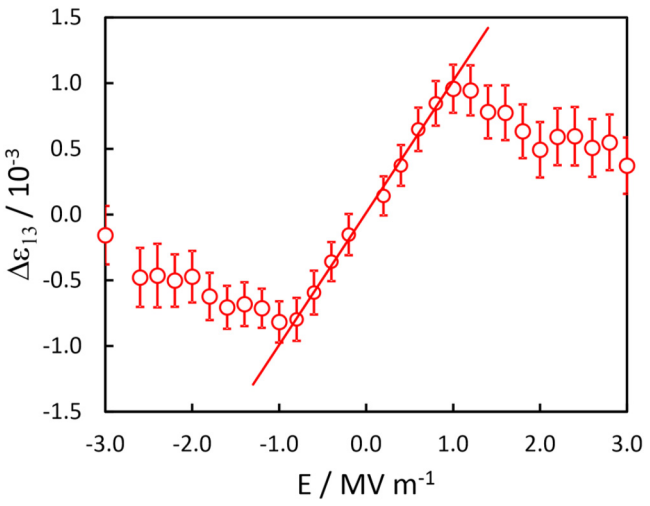

FIG. 9. Variations in electric field-induced shear strain as a function of field level. The linear region was employed to yield an effective piezoelectric coefficient, d_{15}^{*}, of $2.0 \times 10^{-9}\ m\ V^{-1}$.

D. Principal strains: Variations in magnitude and orientation

By fitting the SOD results to the standard relationship shown in Eq. (16), it is now possible to determine the orientation of the principal strain, ψ_p, using the following equation:

$$\tan(\psi_p) = \frac{2\,\varepsilon_{13}}{(\varepsilon_{33} - \varepsilon_{11})}. \quad (17)$$

The results of this procedure are plotted in Fig. 10, which illustrates the ψ_p values obtained both from the total strain, $\varepsilon(\psi)$, and from the strains associated with the individual plane families, $\varepsilon_{hkl}(\psi)$. The value of ψ_p remains close to zero up to an electric field in the region of $0.8\ MV\ m^{-1}$, when a significant increase or decrease occurs, dependent on the sense of the field. The magnitude of ψ_p increases sharply from 7° to 45° in the relatively narrow

field range from 0.6 to 1.4 MV m^{-1} and then continues to increase progressively up to 80° at the maximum field of 3 MV m^{-1}. These data are consistent with the reorientation of ferroelectric domains toward the direction of the applied electric field, X_1. However, the charge displacement mechanisms contribute in different ways to strain and polarization. For example, it is well-established that in the remanent state, 180° domain switching does not contribute to strain, while 90° domain switching does. In contrast, both mechanisms contribute to polarization. Therefore, the principal strain direction, ψ_p, does not necessarily coincide with the direction of the polarization vector. The manner in which the reorientation of polarization occurs depends on the domain switching mechanisms, as discussed below.

It should be noted that the results obtained from individual grain families should not necessarily follow that of the total strain, due to the influence of elastic anisotropy and potentially different coercive fields associated with different grain orientations. However, the influence of elastic coupling can also be observed in the ψ_p–E relationships for the different plane families, plotted in Fig. 10(b), which follow remarkably similar trends.

It was noted above that the directions of the principal strain axis and the average polarization vector are not necessarily correlated due to the nature of different domain switching mechanisms. Two possible scenarios associated with either solely 90° domain switching, or a combination of 90° and 180° domain switching, are presented in Fig. 11. In this figure, the schematic distribution of polarization orientations at different stages of the cross-poling procedure is illustrated on the left-hand side of the diagram while the associated variations in the norm of the polarization, ||P||, the direction of principal strain, ψ_p, and the principal strain values, ε^+ and ε^-, are summarized on the right. The domain orientation distributions at the beginning and end of the process are considered to be the same in each case, but the intermediate state differs.

In the first scenario, the reorientation of polarization under the cross-poling field is supposed to occur solely by 90° domain switching; this results in a progressive increase in ψ_p, while the magnitude of polarization and the principal strain values remain constant. For the second scenario, the reorientation of polarization occurs first by 180° and subsequently by 90° switching; in this case, there is also a progressive increase in ψ_p, but the magnitude of polarization and those of the principal strains suffer a reduction in the intermediate state. The schematic shown in Fig. 11(b) II illustrates the hypothetical case where exclusively 180° domain switching has occurred, in which case the curves representing ε^+ and ε^- could potentially intersect and ε^+ would become less than ε^- in the intermediate state.

The data obtained during the present experiment were used to evaluate the validity of these mechanisms through the principal strain values, which are given by the following relationships:

$$\varepsilon^+ = \frac{\varepsilon_{33}+\varepsilon_{11}}{2} + \sqrt{\left(\frac{\varepsilon_{33}-\varepsilon_{11}}{2}\right)^2 + \varepsilon_{13}^2}, \tag{18}$$

$$\varepsilon^- = \frac{\varepsilon_{33}+\varepsilon_{11}}{2} - \sqrt{\left(\frac{\varepsilon_{33}-\varepsilon_{11}}{2}\right)^2 + \varepsilon_{13}^2}. \tag{19}$$

The results obtained for ε^+ and ε^- are presented in Fig. 12. It is evident that the principal strains do not remain constant after the application of the electric field but reduce slightly in magnitude up to an electric field of around 1 MV m^{-1}. This observation lends

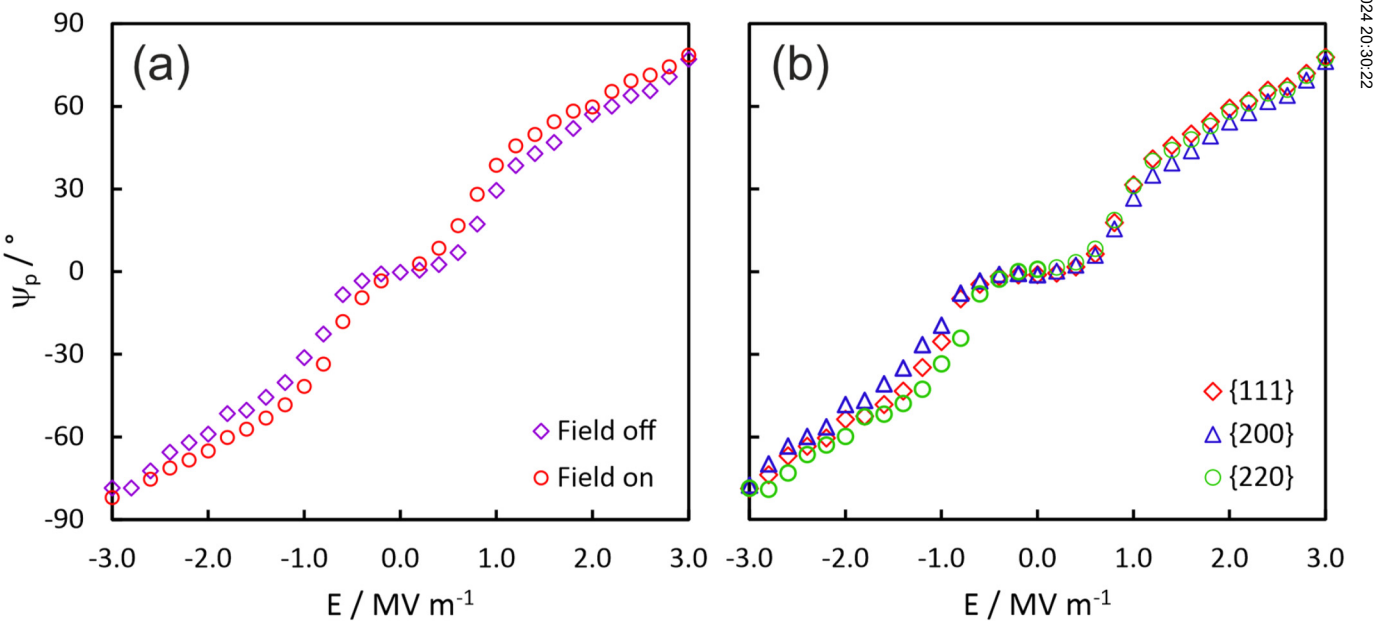

FIG. 10. Changes in the orientation of the principal strain direction, ψ_p, due to an increasing bipolar electric field, determined from (a) total strain and (b) strain of individual plane families in the "field-off" state. Error bars omitted for clarity.

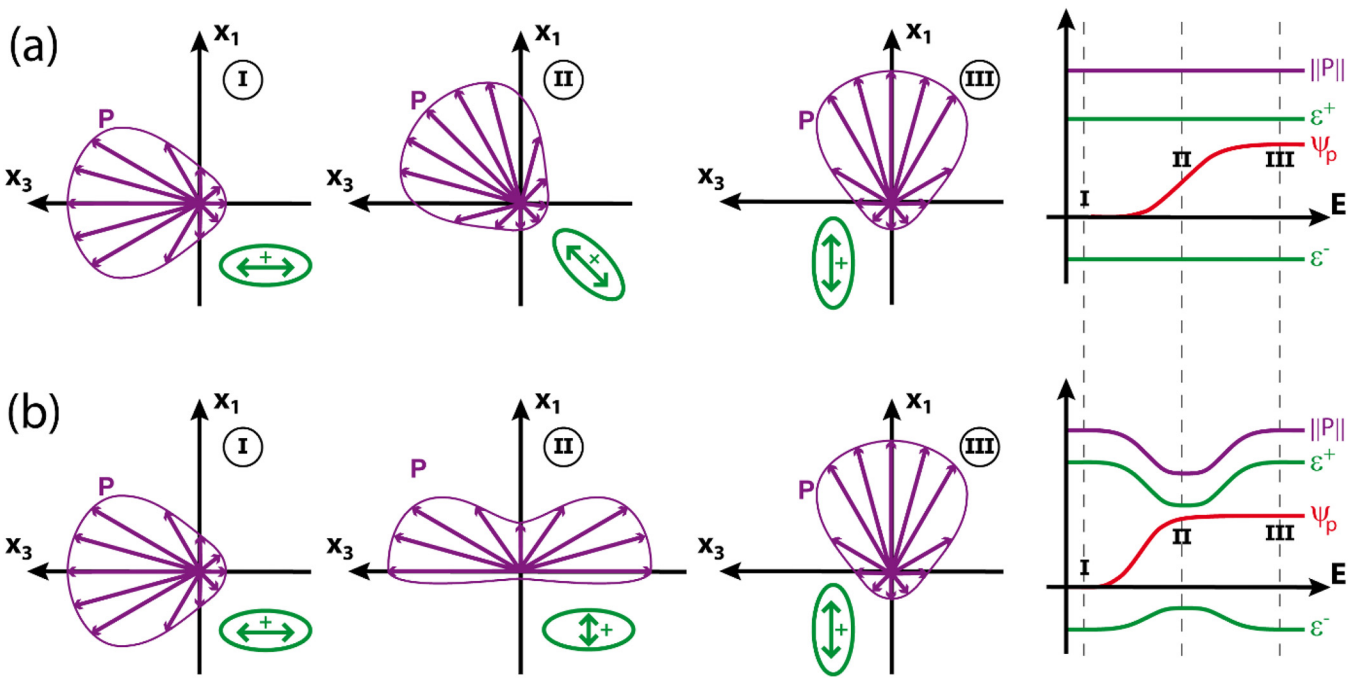

FIG. 11. Schematic illustration of changes in the orientation of polarization and associated principal strain values effected by (a) solely 90° or (b) combined 180° and 90° ferroelectric domain switching.

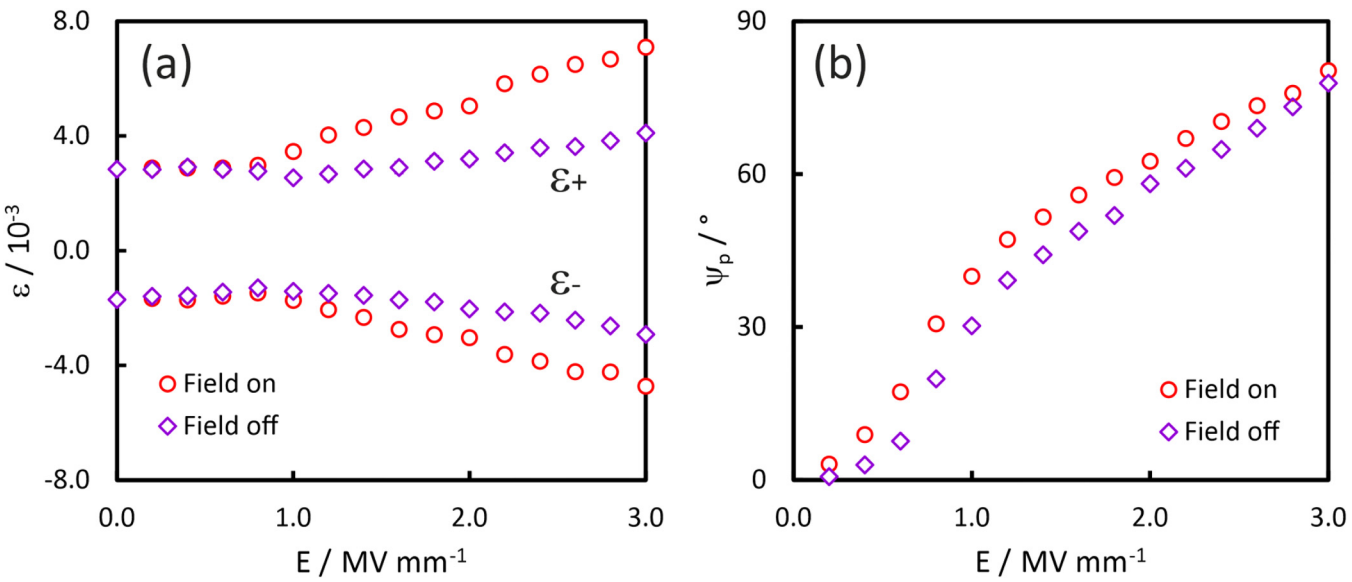

FIG. 12. Variations in (a) the magnitude of total principal strains, averaged over positive (ε^+), and negative (ε^-) field values, in response to an increasing electric field amplitude and (b) the associated changes in the orientation of the principal strain.

support to the suggestion that 180° domain switching provides a significant contribution to the changes in polarization, at least during the initial stages. Simultaneous measurements of the variations in macroscopic strain and polarization during cross-poling would help to clarify this point.

Significant increases in the magnitude of the principal strains occur for field levels above 1 MV m^{-1}, particularly in the "field-on" state, confirming the observations made in Sec. III B with reference to Fig. 7, i.e., the level of strain after cross-poling along the X_1 direction is higher than the strain observed in the initial poled state. This could be a consequence of time-dependent relaxation effects, meaning that some back-switching of domains occurred after the initial poling procedure, perhaps driven by the elastic energy associated with inter-granular residual stress. This would result in a reduction in the remanent polarization in the well-aged initial state relative to that obtained immediately upon cross-poling.

Another significant feature of the results shown in Fig. 12 is that the differences between the principal strains in the "field-on" and "field-off" states increase as the magnitude of the applied field increases, demonstrating that the axial mode becomes increasingly dominant. This is expected to occur as the average polarization vector rotates gradually toward direction X_1. The general correlation between the increasing magnitudes of the *difference strains*, caused by the axial piezoelectric coefficients, and the principal strain direction is shown by the inset in Fig. 12(b).

Further studies are required to determine the variations in the nonlinear dielectric and piezoelectric properties of PZT and other related piezoceramics in the sub-coercive field range at various stages of the cross-poling process. This could be achieved by macroscopic polarization and full-field strain measurements under an applied electric field, for example, using digital image correlation (DIC). Such studies could enable the development of novel actuator designs to exploit the anisotropic electromechanical responses. It is already well-established that certain "rotator" ferroelectrics exhibit pronounced piezoelectric anisotropy,[8] but the influence of inter-granular elastic constraint and ferroelectric domain switching phenomena on the anisotropic electromechanical behavior of polycrystalline piezoceramics have not yet been investigated in depth. The development of suitable models to describe and predict such effects would also be invaluable.

IV. CONCLUSIONS

The influence of an electric field, applied in a direction (X_1) perpendicular to that of the initial remanent polarization (X_3), on ferroelectric domain orientation and lattice strain of a tetragonal PZT ceramic, has been determined using *in situ* high- energy XRD. At low field levels, a reversible piezoelectric response was observed in the shear mode, with negligible axial strains. Higher field amplitudes led to substantial and irreversible changes in both axial and shear strains associated with ferroelectric domain switching and subsequent reorientation of the average polarization direction toward that of the electric field.

The axial strains increased progressively for field levels beyond the coercive field, while the shear strain first increased and then reduced as the polarization vector became better-aligned with the electric field. The elongations associated with specific lattice directions, expressed in terms of an effective weighted average strain, $\varepsilon_{\{hkl\}}$, exhibited strong anisotropy, with the highest values being obtained for $\varepsilon_{\{200\}}$, the lowest for $\varepsilon_{\{111\}}$, and $\varepsilon_{\{220\}}$ being intermediate. However, the orientations associated with the maxima and minima in the SOD function remained well correlated as they evolved during the cross-poling process due to the influence of elastic coupling between grains in the polycrystalline matrix.

The rotation of the average polarization direction was monitored in terms of the principal strain axis, although it is noted that the two are not necessarily coincident. Variations in the magnitudes of the principal strains suggest that the degree of domain alignment was improved in the final stages of the cross-poling procedure, although the reorientation of the principal strain axis toward the electric field was incomplete.

SUPPLEMENTARY MATERIAL

See the supplementary material for the following additional data plots: (i) contour plots to illustrate the evolution of representative diffraction peak profiles under the applied bipolar electric field for azimuthal angles, ψ, of 0°, 45°, and 135°; (ii) contour plots demonstrating the variations in representative diffraction peak profiles as a function of ψ in the final remanent state, after the application of the cross-poling electric field; and (iii) the electric field-dependence of the principal strain components, ε_{33}, ε_{11}, and ε_{13} for the representative crystal orientations.

ACKNOWLEDGMENTS

We acknowledge Diamond Light Source for access to beamline I15 (EE8699) that contributed to the results presented here. This work was supported at the University of Manchester by the Engineering and Physical Sciences Research Council (EPSRC) under Grant No. EP/J010685/1 and by the EPSRC/Xaar Ltd. Impact Acceleration Account, code IAA020. D.A.H. acknowledges CentraleSupelec and the Group of Electrical Engineering Paris (GeePs) for Invited Professorship.

AUTHOR DECLARATIONS

Conflict of interest

The authors have no conflicts to disclose.

Author Contributions

D. A. Hall: Conceptualization (equal); Data curation (equal); Formal analysis (equal); Funding acquisition (equal); Investigation (equal); Methodology (equal); Visualization (equal); Writing – original draft (equal); Writing – review & editing (equal). **L. Daniel:** Conceptualization (equal); Formal analysis (equal); Funding acquisition (equal); Investigation (equal); Methodology (supporting); Software (equal); Visualization (supporting); Writing – original draft (supporting); Writing – review & editing (supporting). **M. Watson:** Funding acquisition (supporting); Project administration (supporting); Writing – review & editing (supporting). **A. Condie:** Funding acquisition (equal); Project administration (supporting); Resources (supporting); Writing – review & editing (supporting). **T. P. Comyn:** Conceptualization

(equal); Funding acquisition (supporting); Investigation (supporting); Supervision (supporting); Validation (supporting); Writing – review & editing (supporting). **A. K. Kleppe:** Data curation (supporting); Investigation (supporting); Methodology (supporting); Project administration (supporting); Resources (supporting); Software (supporting); Validation (supporting); Writing – review & editing (supporting). **P. J. Withers:** Funding acquisition (supporting); Methodology (supporting); Project administration (supporting); Supervision (supporting); Writing – review & editing (supporting).

DATA AVAILABILITY

The data that support the findings of this study are available from the corresponding author upon reasonable request.

REFERENCES

[1]K. Uchino, "Materials issues in design and performance of piezoelectric actuators: An overview," Acta Mater. **46**(11), 3745–3753 (1998).
[2]G. H. Haertling, "Ferroelectric ceramics: History and technology," J. Am. Ceram. Soc. **82**, 797–818 (1999).
[3]S. Gebhardt, L. Seffner, F. Schlenkrich, and A. Schönecker, "PZT thick films for sensor and actuator applications," J. Eur. Ceram. Soc. **27**(13–15), 4177–4180 (2007).
[4]W. Heywang, K. Lubitz, and W. Wersing, *Piezoelectricity : Evolution and Future of a Technology* (Springer, 2008).
[5]R. Dittmer, K. G. Webber, E. Aulbach, W. Jo, X. Tan, and J. Rödel, "Optimal working regime of lead–zirconate–titanate for actuation applications," Sens. Actuators, A **189**, 187–194 (2013).
[6]E. F. Crawley and J. De Luis, "Use of piezoelectric actuators as elements of intelligent structures," AIAA J. **25**, 1373–1385 (1987).
[7]Z. c. Qiu, J. d. Han, X. m. Zhang, Y. c. Wang, and Z. w. Wu, "Active vibration control of a flexible beam using a non-collocated acceleration sensor and piezoelectric patch actuator," J. Sound Vib. **326**(3), 438–455 (2009).
[8]M. Davis, M. Budimir, D. Damjanovic, and N. Setter, "Rotator and extender ferroelectrics: Importance of the shear coefficient to the piezoelectric properties of domain-engineered crystals and ceramics," J. Appl. Phys. **101**(5), 054112 (2007).
[9]M. Hagiwara, T. Hoshina, H. Takeda, and T. Tsurumi, "Nonlinear shear responses of lead zirconate titanate piezoelectric ceramics," Jpn. J. Appl. Phys. **49**(9), 09MD04 (2010).
[10]A. J. Moulson and J. M. Herbert, *Electroceramics Materials, Properties, Applications* (Wiley, 2003).
[11]M. H. Malakooti and H. A. Sodano, "Shear mode energy harvesting of piezoelectric sandwich beam," Proc. SPIE **8688**, 86881R (2013).
[12]J. Brünahl and A. M. Grishin, "'Piezoelectric shear mode drop-on-demand inkjet actuator,' Sens. Actuators, A **101**(3), 371–382 (2002).
[13]V. Mueller and Q. M. Zhang, "Shear response of lead zirconate titanate piezoceramics," J. Appl. Phys. **83**(7), 3754–3761 (1998).
[14]F. X. Li, D. N. Fang, and Y. M. Liu, "Domain switching anisotropy in poled lead titanate zirconate ceramics under orthogonal electromechanical loading," J. Appl. Phys. **100**(8), 1–6 (2006).
[15]Y. M. Liu, F. X. Li, and D. N. Fang, "Anisotropy of domain switching in pre-poled lead titanate zirconate ceramics under multiaxial electrical loading," Appl. Phys. Lett. **90**, 032905 (2007).
[16]M. H. Malakooti and H. A. Sodano, "Direct measurement of piezoelectric shear coefficient," J. Appl. Phys. **113**(21), 214106 (2013).
[17]D. Damjanovic, "Stress and frequency dependency of the direct piezoelectric effect in ferroelectric ceramics," J. Appl. Phys. **82**(4), 1788–1797 (1997).
[18]D. A. Hall, "Review nonlinearity in piezoelectric ceramics," J. Mater. Sci. **36**(19), 4575–4601 (2001).
[19]R. E. Eitel, T. R. Shrout, and C. A. Randall, "Nonlinear contributions to the dielectric permittivity and converse piezoelectric coefficient in piezoelectric ceramics," J. Appl. Phys. **99**(12), 1–7 (2006).
[20]J. E. Garcia, R. Perez, A. Albareda, and J. A. Eiras, "Extrinsic response anisotropy in ferroelectric perovskite polycrystals," Solid State Commun. **144**(1–2), 23–26 (2007).
[21]P. J. Stevenson and D. A. Hall, "The effect of grain size on the high field dielectric properties of hard PZT ceramics," Ferroelectrics **223**(1), 309–318 (1999).
[22]D. Berlincourt, "Piezoelectric ceramic compositional development," J. Acoust. Soc. Am. **91**(5), 3034–3040 (1992).
[23]J. Rödel, W. Jo, K. T. P. Seifert, E. M. Anton, T. Granzow, and D. Damjanovic, "Perspective on the development of lead-free piezoceramics," J. Am. Ceram. Soc. **92**(6), 1153–1177 (2009).
[24]M. Hagiwara, S. Takahashi, T. Hoshina, H. Takeda, O. Sakurai, and T. Tsurumi, "Nonlinear shear response in (K,Na)NbO_3-based lead-free piezoelectric ceramics," Key Eng. Mater. **445**, 47–50 (2010).
[25]Z. Tan, J. Xing, Y. Peng, Q. Zhang, and J. Zhu, "Polarization rotation boosts strong piezoelectric response in the lead-free perovskite ferroelectric $K_{0.5}Na_{0.5}NbO_3$," Phys. Rev. B **104**, 014104 (2021).
[26]K. Shibata, R. Wang, T. Tou, and J. Koruza, "Applications of lead-free piezoelectric materials," MRS Bull. **43**(8), 612–616 (2018).
[27]J. Yin, V. K. Wong, Q. Xu, P. T. C. Subhodayam, Y. M. Yousry, A. Shashidhara, J. Zhou, P. Luo, P. C. Lim, F. X. Wei, D. B. K. Lim, C. Sun, and K. Yao, "Conformable shear mode transducers from lead-free piezoelectric ceramic coatings: An innovative ultrasonic solution for submerged structural health monitoring," Adv. Funct. Mater. **2401544**, 1–10 (2024).
[28]A. Endriss, M. Hammer, M. J. Hoffmann, A. Kolleck, and G. A. Schneider, "Microscopic and macroscopic ferroelectric–ferroelastic and piezoelectric behavior of PZT ceramics," J. Eur. Ceram. Soc. **19**(6–7), 1229–1231 (1999).
[29]D. A. Hall, A. Steuwer, B. Cherdhirunkorn, T. Mori, and P. J. Withers, "A high energy synchrotron x-ray study of crystallographic texture and lattice strain in soft lead zirconate titanate ceramics," J. Appl. Phys. **96**(8), 4245–4252 (2004).
[30]J. L. Jones, M. Hoffman, and S. C. Vogel, "Ferroelastic domain switching in lead zirconate titanate measured by *in situ* neutron diffraction," Mech. Mater. **39**(4), 283–290 (2007).
[31]J. L. Jones, "The use of diffraction in the characterization of piezoelectric materials," J. Electroceram. **19**(1), 69–81 (2007).
[32]M. Hinterstein, M. Hoelzel, J. Rouquette, J. Haines, J. Glaum, H. Kungl, and M. Hoffman, "Interplay of strain mechanisms in morphotropic piezoceramics," Acta Mater. **94**, 319–327 (2015).
[33]D. A. Hall, A. Steuwer, B. Cherdhirunkorn, P. J. Withers, and T. Mori, "Micromechanics of residual stress and texture development due to poling in polycrystalline ferroelectric ceramics," J. Mech. Phys. Solids **53**(2), 249–260 (2005).
[34]D. A. Hall, T. Mori, P. J. Withers, H. Kungl, M. J. Hoffmann, and J. Wright, "Domain switching in rhombohedral PZT ceramics under electrical and mechanical loading," Mater. Sci. Technol. **24**(8), 927–933 (2008).
[35]A. Pramanick, J. E. Daniels, and J. L. Jones, "Subcoercive cyclic electrical loading of lead zirconate titanate ceramics II: Time-resolved x-ray diffraction," J. Am. Ceram. Soc. **92**(10), 2300–2310 (2009).
[36]J. E. Daniels, M. Majkut, Q. Cao, S. Schmidt, J. Wright, W. Jo, and J. Oddershede, "Heterogeneous grain-scale response in ferroic polycrystals under electric field," Sci. Rep. **6**, 1–7 (2016).
[37]J. E. Daniels, W. Jo, J. Rödel, and J. L. Jones, "Electric-field-induced phase transformation at a lead-free morphotropic phase boundary. Case study in a 93%($Bi_{0.5}Na_{0.5}$)TiO_3-7% $BaTiO_3$ piezoelectric ceramic," Appl. Phys. Lett. **95**(3), 032904 (2009).
[38]W. Jo, J. E. Daniels, J. L. Jones, X. Tan, P. a. Thomas, D. Damjanovic, and J. Rödel, "Evolving morphotropic phase boundary in lead-free ($Bi_{1/2}Na_{1/2}$)TiO_3–$BaTiO_3$ piezoceramics," J. Appl. Phys. **109**, 014110 (2011).

[39]A. J. Royles, A. J. Bell, J. E. Daniels, S. J. Milne, and T. P. Comyn, "Observation of a time-dependent structural phase transition in potassium sodium bismuth titanate," Appl. Phys. Lett. **98**(18), 3–5 (2011).
[40]K. Y. Lee, X. Shi, N. Kumar, M. Hoffman, M. Etter, J. Winter, L. Lemos Da Silva, D. Seifert, and M. Hinterstein, "The complex structural mechanisms behind strain curves in bismuth sodium titanate-barium titanate," Appl. Phys. Lett. **116**, 182902 (2020).
[41]S. Wan and K. J. Bowman, "Cross-poling textures in a lead zirconate titanate piezoelectric material," J. Mater. Res. **15**(6), 1248–1249 (2000).
[42]A. P. Hammersley, S. O. Svensson, M. Hanfland, A. N. Fitch, and D. Hausermann, "Two-dimensional detector software: From real detector to idealised image or two-theta scan," High Press. Res, **14**(4–6), 235–248 (1996).
[43]J. L. Jones, E. B. Slamovich, and K. J. Bowman, "Domain texture distributions in tetragonal lead zirconate titanate by x-ray and neutron diffraction," J. Appl. Phys. **97**(3), 1–6 (2005).
[44]L. Daniel, D. A. Hall, J. Koruza, K. G. Webber, A. King, and P. J. Withers, "Revisiting the blocking force test on ferroelectric ceramics using high energy x-ray diffraction," J. Appl. Phys. **117**(17), 174104 (2015).
[45]A. Pramanick, D. Damjanovic, J. E. Daniels, J. C. Nino, and J. L. Jones, "Origins of electro-mechanical coupling in polycrystalline ferroelectrics during subcoercive electrical loading," J. Am. Ceram. Soc. **94**(2), 293–309 (2011).
[46]M. T. Hutchings, P. J. Withers, T. M. Holden, and T. Lorentzen, *Introduction to the Characterization of Residual Stress by Neutron Diffraction* (Taylor & Francis, 2005).
[47]M. R. Daymond, "The determination of a continuum mechanics equivalent elastic strain from the analysis of multiple diffraction peaks," J. Appl. Phys. **96**(8), 4263–4272 (2004).
[48]J. E. Daniels, T. R. Finlayson, A. J. Studer, M. Hoffman, and J. L. Jones, "Time-resolved diffraction measurements of electric-field-induced strain in tetragonal lead zirconate titanate," J. Appl. Phys. **101**(9), 094104 (2007).
[49]L. Daniel, D. A. Hall, K. G. Webber, A. King, and P. J. Withers, "Identification of crystalline elastic anisotropy in PZT ceramics from in-situ blocking stress measurements," J. Appl. Phys. **115**, 174102 (2014).
[50]J. F. Nye, *Physical Properties of Crystals: Their Representation by Tensors and Matrices* (Clarendon Press, 1985).